Simulating a Chemically-Fueled Molecular Motor with Nonequilibrium Molecular Dynamics

Alex Albaugh¹ and Todd R. Gingrich¹

¹Department of Chemistry, Northwestern University, 2145 Sheridan Road, Evanston, Illinois 60208, USA

Most computer simulations of molecular dynamics take place under equilibrium conditions—in a closed, isolated system, or perhaps one held at constant temperature or pressure. Sometimes, extra tensions, shears, or temperature gradients are introduced to those simulations to probe one type of nonequilibrium response to external forces. Catalysts and molecular motors, however, function based on the nonequilibrium dynamics induced by a chemical reaction's thermodynamic driving force. In this scenario, simulations require chemostats capable of preserving the chemical concentrations of the nonequilibrium steady state. We develop such a dynamic scheme and use it to observe cycles of a new particle-based classical model of a catenane-like molecular motor. Molecular motors are frequently modeled with detailed-balance-breaking Markov models, and we explicitly construct such a picture by coarse graining the microscopic dynamics of our simulations in order to extract rates. This work identifies inter-particle interactions that tune those rates to create a functional motor, thereby yielding a computational playground to investigate the interplay between directional bias, current generation, and coupling strength in molecular information ratchets.

Molecular motors are ubiquitous in biology. Proteins like kinesin [1] and myosin [2] transduce free energy, hydrolyzing adenosine triphosphate (ATP) to power mechanical work [3–6]. These motors operate by coupling ATP hydrolysis to linear motion, carrying cellular cargoes along microtubule and actin tracks, respectively. Those natural motors have also been engineered to modify their performance. Mutated kinesin can process further along microtubule tracks than wild type [7, 8] or rapidly cease activity in response to small molecules [9]. Myosin can be engineered to move along an actin track in the opposite direction of the wild type motor [10, 11]. Despite those successes modifying existing motors, it remains challenging to design molecular interactions to build similar machines from the ground up.

Chemists have sought to build those machines using the principles of the biological motors but with different synthetic building blocks [12–14]. Like the biological inspiration, the synthetic machines should rectify thermal fluctuations into directed motion by harvesting free energy from chemical fuel, a goal first realized by the artificial motor of Wilson et al. [15]. One challenge in designing these machines is that the mechanism is typically considered in terms of the kinetics of elementary steps while the design is more naturally thought of in terms of the strength of interactions between molecular components. Connecting those interactions to the ultimate dynamical function is particularly challenging because microscopic motors operate in a noisy regime characterized by stochastic fluctuations [16, 17].

In equilibrium situations, computer simulations have proven to be particularly useful at bridging that connection between molecular design and dynamics, particularly in the presence of noise [18]. The nonequilibrium dynamics of molecular motors, however, preclude straightforward application of equilibrium simulation methods. Equilibrium dynamics moves in forward and reverse directions with equal probability, so a directional motor re-

quires nonequilibrium conditions powered by a chemical fuel [3, 6, 19, 20]. To capture the nonequilibrium behavior in simulations, a number of different strategies have been employed. One approach aims to describe different equilibria of a motor, e.g., one with a fuel bound and one with the fuel unbound. The nonequilibrium dynamics is induced by externally imposing time-dependent swaps between these energy surfaces [21–27]. A complementary body of work breaks the time-reversal symmetry of equilibrium dynamics by imposing forces or torques on the motor [28–33]. Both approaches can obscure how the chemistry couples to the mechanical motion, and that mechanochemical coupling is central to a motor's function [6, 34]. To explicitly capture that coupling, it is necessary to continually resupply fuel and extract waste from a simulation so as to sustain a nonequilibrium steady state, a strategy implemented with a minimal kinesin-like walker model [35] and with Janus particles and spheredimers motor models that move along self-induced concentration gradients (diffusiophoresis) [36–39].

Here we aimed to develop and simulate a model motor and fuel with sufficiently simple pair potentials that the steady-state dynamics could be directly simulated, with a nonequilibrium environment maintained by external baths. In other words, our motor and fuel undergo microscopically reversible Langevin dynamics with nonequilibrium steady state conditions imposed by grand canonical Monte Carlo (GCMC) chemostats [18, 40]. Our motor is essentially that of Wilson et al. [15], while the "chemical reaction" of our fuel is the escape of a particle that is metastably trapped inside a tetrahedral cluster. Though the reaction is formally reversible, escape is very strongly favored, so the chemostats tend to inject unreacted fuel while removing the reacted waste products. Meanwhile, the Langevin dynamics of the motor's interaction with the fuel are preserved by restricting the GCMC chemostat moves to occur far from the motor. This construction allows us to capture the manner in which nonequilibrium concentrations of fuel and waste couple to the motion of the motor. Armed with the explicit particle-based model, we analyze the resulting currents using a nonequilibrium Markov state framework, with which we aim to more directly connect the stochastic thermodynamic analysis of motors [41–43] with particle-based simulations. The model and methods we report serve as a testbed for exploring how inter-particle interactions affect the operation of a molecular motor.

Fueling a Nonequilibrium Steady State

Consider the dynamics of a motor protein in the presence of ATP, adenosine diphosphate (ADP), and inorganic phosphate (P). In an ideal solution, the reversible chemical reaction ATP \rightleftharpoons ADP + P will relax into an equilibrium with equilibrium constant

$$K = \frac{[\text{ADP}][P]}{[\text{ATP}]} = e^{-\beta(\mu_{\text{ADP}}^0 + \mu_{\text{P}}^0 - \mu_{\text{ATP}}^0)}, \tag{1}$$

where $\mu_{\mathrm{ADP}}^{0},\,\mu_{\mathrm{P}}^{0},$ and μ_{ATP}^{0} are standard-state chemical potentials and β is the inverse temperature in units of Boltzmann's constant $k_{\rm B}$. At chemical equilibrium, the motion of the motor must obey detailed balance, precluding the protein from exhibiting net motion. The situation is altered if external means prevent the chemical reaction from reaching equilibrium, for example, if ATP is fed into the system while ADP and P are extracted. Provided the reaction of ATP is suitably coupled to the protein's motion, the fuel's free energy gradient pushes the motor into a nonequilibrium steady state (NESS) with net directed motion, giving rise to currents. In so-called tightly coupled motors, each reaction event correlates with a configurational change of the motor. For example, when F_1 -ATP synthase generates work from ATP [44], each catalyzed ATP hydrolysis corresponds almost one-to-one with a 120° rotation of a rotor [45]. Other motors are loosely coupled, with motor motion only weakly correlated with fuel consumption [46].

That mechano-chemical coupling can be realized in a strictly classical model, provided the model exhibits a reversible transformation between fuel and waste and that a continuous influx of fuel and outflow of waste prevents relaxation to equilibrium. It is furthermore necessary that the model fuel exhibit metastability, so that interconversion between fuel and waste is slower than fuel injection and waste removal. Because the statistical consequences of nonequilibrium driving forces are present even in strictly classical dynamics, it is not necessary to confront the quantum-mechanical complexities presented by chemical bond breaking. Rather, the classical model suffices as a practical way to address fundamental questions about the impact of pairwise interactions on dynamical function.

A Classical Fuel Model

We constructed the classical fuel out of tetrahedral clusters of volume-excluding particles, as shown in Fig. 1. Four such particles, colored blue, are bonded together to form a tetrahedral shell. A single unbound volumeexcluding particle, colored red, can be kinetically trapped inside the tetrahedron. A filled tetrahedral cluster (FTC) does not retain its red central particle (C) indefinitely. Rather, a rare thermal fluctuation inevitably allows the tetrahedral cluster to contort enough for the kinetically trapped C to escape, leaving behind an empty tetrahedral cluster (ETC). Consistent with microscopic reversibility, the reverse process is also possible. At equilibrium, the flux from FTC \rightarrow ETC + C would balance the reverse flux of ETC + C \rightarrow FTC. Since the ETC + C state is both entropically and energetically favorable, equilibrium would strongly favor the empty tetrahedra. An initial concentration of FTC fuel would quickly deplete to its near-zero equilibrium concentration if not for GCMC chemostats, which provide a mechanism to hold the chemical potentials for the three different species at unequilibrated values. Consequently, within a simulation cell, the FTC, ETC, and C species are stochastically injected and removed so as to maintain a NESS in which the FTC \rightarrow ETC + C reaction is typical. The reverse reaction, though possible, is practically unobserved.

A Classical Motor Model

We aimed to engineer a model motor capable of harvesting the free energy of a NESS with a high concentration of FTC and low concentrations of ETC and C, motivated by the first synthetic, autonomous, chemicallyfueled molecular motor of Wilson et al. [15]. Their motor is a catenane consisting of two interlocked rings. The smaller of the two rings, a benzylic amide, shuttles around a track formed by the larger ring. that track, Wilson et al. engineered two fumaramide binding sites as well as two adjacent hydroxyl groups that catalyze the decomposition of a bulky fuel (9fluorenylmethoxycarbonyl chloride) into waste products (CO₂ and dibenzofulvene). The relative positioning of binding and catalytic sites breaks symmetry such that fuel reaction induces directed motion, the kinetics of which have been expressed elegantly in terms of an information ratchet [47, 48], where directed motion arises from the gating of natural thermal diffusion in a preferred direction [3, 49–51]. That mechanism relies on steric considerations; the fuel reacts more slowly at a catalytic site when the shuttling ring is near enough to block access to the catalytic site. The same sort of mechanism underlies our coarse-grained, classical design. The kinetics of catalvzed fuel reactions must be sensitive to the proximity of the shuttling ring.

In our model, that need is satisfied by introducing intermolecular interactions between the shuttling ring and

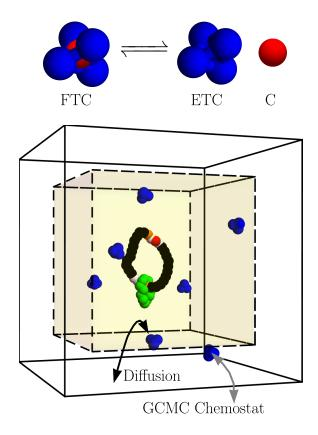


FIG. 1. (top) A tetrahedral cluster formed from two types of particles can transition between filled tetrahedral cluster (FTC) and empty tetrahedral cluster (ETC) plus central particle (C) states while executing Langevin dynamics at a fixed temperature. Chemical potentials for each species $(\mu_{\rm FTC}, \mu_{\rm ETC}, \text{ and } \mu_{\rm C})$ are regulated with grand canonical Monte Carlo chemostats to drive the reaction away from equilibrium. (bottom) A simulation cell containing a model motor driven at the nonequilibrium steady state fuel concentrations. The motor is constrained to occupy the inner box (shaded yellow) through a Lennard-Jones wall potential while the GCMC chemostats insert and remove FTC, ETC, and C only from the outer box (white background). FTC, ETC, and C do not experience the Lennard-Jones wall potential and freely diffuse between the inner and outer boxes. The motor consists of a small shuttling ring (green particles) that diffuses around a larger ring composed of two shuttling-ring-binding sites (orange particles), each adjacent to a three-particle catalytic site (white particles). The remainder of the larger ring is made of inert particles (black) that only have mildly repulsive interactions with other particles. The catalytic sites speed up the FTC \rightarrow ETC + C decomposition due to attractions between white catalytic particles and the blue and red particles of FTC. Upon their escape, the red C particles can linger around the catalytic sites, blocking the shuttling ring and ultimately gating diffusion to generate net directed current.

the components of the model fuel. As described briefly in Fig. 1 and more thoroughly in Methods, we construct a motor from two interlocking rings of particles. The smaller green ring has attractive interactions with orange binding sites on the larger ring. The particles of FTC,

ETC, and C molecules have interactions that encourage the FTC \rightarrow ETC + C reaction at the white catalytic sites. Following the reaction, the C particle remains at the catalytic site as a blocking group, which the shuttling ring cannot diffuse past. Proximity of the shuttling ring to a catalytic site decreases the rate of catalysis relative to the distal catalytic site. This imbalance of rates, along with the nonequilibrium replenishment of FTC and removal of ETC and C, yields net directed motion when the pair potentials are suitably tuned, a point we return to in a more detailed discussion of the mechanism.

Dynamics

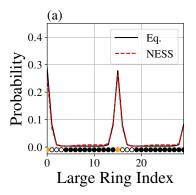
The dynamics of the fueled motor were evolved in time by mixing the Langevin dynamics of the particles with GCMC chemostats that maintained the NESS. The Langevin equations of motion for each particle i is

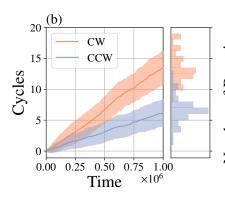
$$\dot{\mathbf{r}}_{i} = \frac{\mathbf{p}_{i}}{m_{i}}$$

$$\dot{\mathbf{p}}_{i}(t) = -\nabla U(\mathbf{r}_{i}(t)) - \frac{\gamma}{m_{i}}\mathbf{p}_{i}(t) + \boldsymbol{\xi}_{i}(t),$$
(2)

where γ is the friction coefficient, \mathbf{p}_i is the momentum of particle i, \mathbf{r}_i is the position of particle i, m_i is the mass of that particle, U is the potential energy, and $\boldsymbol{\xi}_i$ is white noise with $\langle \boldsymbol{\xi}_i \rangle = \mathbf{0}$ and $\langle \boldsymbol{\xi}_i(t)\boldsymbol{\xi}_i(t') \rangle = 2\gamma k_{\rm B}T\delta(t-t')$ at temperature T. All model parameters are reported in non-dimensional units as described in Methods.

The simulation box consists of two concentric cubes with an inner cube and an outer cube, shown in Fig. 1. GCMC moves occur between the inner and outer boxes and serve to insert and remove FTC, ETC, and C from the system. The motor itself (the two interlocked rings) is confined to the inner box with a wall potential, but the wall potential is not applied to the FTC, ETC, or C molecules, which freely diffuse between the two boxes and can cross the periodic boundaries of the outer box. Since GCMC insertions and deletions occur in the space between the inner and outer box and the motor is confined to the inner box, the motor will not be directly affected by the GCMC moves. However, the motor does feel the indirect effect of the nonequilibrium concentrations since the timescale for diffusion is fast compared to the lifetime of the FTC. After every 100 time steps of Langevin dynamics, a GCMC trial move is chosen uniformly from six options—an insertion or deletion of the three species, FTC, ETC, or C. These moves are conditionally accepted with a Metropolis factor that depends on the set chemical potentials of the three species and their instantaneous concentrations. As described in Methods and the SI, the GCMC procedure must account for the internal degrees of freedom of the FTC and ETC clusters [40, 52]. Due to those internal degrees of freedom, the GCMC acceptance probabilities directly depend on $\mu' \equiv \mu - A^0$, the applied external chemical potential less the standard state Helmholtz free energy. The strongly driven regime corresponds to having a high μ'_{FTC} but a low μ'_{ETC} and μ'_{C} .





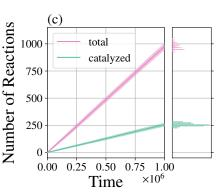


FIG. 2. Behavior of Motor II with $\mu'_{\rm FTC} = 0.5$, $\mu'_{\rm ETC} = -10$, and $\mu'_{\rm C} = -10$ corresponding to an average of about 8.5 FTC molecules, 0.1 ETC molecules, and 0.9 C particles in the simulation box. (a) The distribution for the shuttling ring position, measured as the index of large ring particle nearest to the shuttling ring center of mass, for NESS and equilibrium (Eq.) conditions in the absence of FTC, ETC, and C. An unfolded schematic of the large ring is superimposed over the particle indices to visualize the particle types at each location around the large ring. Orange particles are binding sites, white particles are catalytic sites, and black particles are inert. (b) In the NESS conditions, the shuttling ring executes more clockwise (CW, orange) than counterclockwise (CCW, blue) cycles around the large ring when measured in the frame of the large ring. (c) Decomposition reactions FTC \rightarrow ETC + C include those catalyzed by the motor (green) and spontaneous reactions in the bulk, which combine to give the total (pink). Decompositions occurring within 2 units of a white catalytic particle are classified as having been catalyzed by the motor. Means and standard deviations are generated from 50 independent simulations for each motor.

Under those conditions, the typical process starts by inserting FTC into the outer box. This FTC diffuses into the inner box where it interacts with the motor and gets converted into ETC and C. These waste products then diffuse back into the outer box where they are removed by the GCMC chemostats.

Accuracy, Current, and Coupling Efficiency

The motor and fuel models are characterized by numerous parameters controlling the form and strength of pairwise interactions. We first discovered parameters for the fuel that resulted in the desired metastability of the FTC state. Subsequently, we scanned parameter spaces to identify the interactions between motor and fuel that would reliably generate current, landing upon two sets of interactions, herein referred to as Motor I and Motor II. These two motors differ only subtly; Motor I features slightly stronger attractions between the shuttling ring and binding and also between the C particles and the catalytic site. The full parameterization of both motors can be found in Section D of the SI.

The behavior of Motor II in an underdamped regime $(\gamma=0.5)$ with a moderate driving force is shown in Fig. 2 (see also SI Movie 1). The NESS fuel concentration only slightly alters the distribution of the motor configurations relative to thermal equilibrium with no FTC, ETC, or C present. In both cases, the steady-state location of the shuttling ring concentrates around the binding sites. Despite that similarity between the equilibrium and NESS stationary distributions, the NESS dynamical behavior

deviates markedly from equilibrium. In the presence of the NESS driving, the total number of clockwise (CW) and counterclockwise (CCW) cycles do not balance, corresponding to net current. Figure 2 also reflects two important manners in which the present model motor differs from biological machines like ATP synthase. Firstly, our motor is fairly loosely coupled—Figs. 2b and 2c show that a single net cycle requires roughly 35 catalyzed FTC \rightarrow ETC + C reactions. Secondly, the model fuel is less deeply metastable than ATP. Even in the absence of a motor's catalytic site, FTC can degrade on simulation timescales. As such, Fig. 2c distinguishes between catalyzed decompositions that occur in proximity to the catalytic sites and the total decompositions that could occur elsewhere.

In Fig. 3, we report how adding more fuel increases the CW bias, increases the current, and decreases the coupling. Those three measures of motor performance were calculated by monitoring the number of clockwise and counterclockwise shuttling ring cycles, $n_{\rm CW}$ and $n_{\rm CCW}$, respectively. If the motor's goal is to generate CW cycles then one measure of accuracy is the CW bias, the fraction of cycles in the CW direction:

$$\frac{n_{\rm CW}}{n_{\rm CW} + n_{\rm CCW}}. (3)$$

The current, the net cycles per time, is similarly computed from $n_{\rm CW}$ and $n_{\rm CCW}$ as

$$\frac{n_{\rm CW} - n_{\rm CCW}}{t_{\rm obs}},\tag{4}$$

where $t_{\rm obs} = N_{\rm steps} \Delta t$ is the observed simulation time and $N_{\rm steps}$ is the number of simulation time steps of size

 Δt . Finally, the coupling between catalyzed reaction and net CW cycles is

$$\frac{n_{\rm CW} - n_{\rm CCW}}{n_{\rm cat}},\tag{5}$$

where n_{cat} counts the number of FTC decompositions occurring with center of mass within 2 units of a catalytic particle.

Both motors exhibit similar responses to changes in FTC concentration, illustrating a tradeoff: greater bias comes at the expense of lower current and lower coupling. We anticipated a maximum coupling of 0.5, corresponding to a tightly coupled cycle with one catalyzed reaction at each catalytic site. Neither motor achieves that limit. Rather, they are loosely coupled, with catalyzed reactions probabilistically gating diffusion and inducing no major conformational changes in the motor itself. Though the coupling efficiency of these motors is about one order of magnitude below the maximum, we find it encouraging that such a crudely designed toy model can nevertheless convert roughly 1/10 of the catalyzed reactions into directed current.

Since we have described simulations in the underdamped regime ($\gamma=0.5$), it is natural to wonder if the motor's current is dependent on inertia. Figure 4 shows that the current generation indeed persists in an overdamped regime ($\gamma=10$) more reflective of the viscous low Reynolds number environment experienced by in vivo biological motors. While increased damping reduces the current by an order of magnitude, it also causes the CW bias of both motors to increase, with Motor I approaching 100%.

An Eight-State Rate Model

To rationalize the dynamics of the explicit NESS simulations, it is productive to analyze the rates for transitioning between discrete coarse-grained states. Inspired by a simple six-state Markov model [47, 48] that captures the mechanism of the Wilson et al. motor [15], we harvested our simulation data to collect statistics of the transition times between the eight coarse-grained states depicted in Fig. 5. Those states are determined by three bits of information: (1) which half of the large ring is nearest the shuttling ring center of mass, (2) whether the first catalytic site is blocked, and (3) whether the second catalytic site is blocked, with blockage defined as having at least one free C within 1.2 distance units of a catalytic site's middle particle.

Due to the symmetry of the problem, we focus on seven rates for transitions between these eight states: $k_{\rm CW}$ and $k_{\rm CCW}$ for CW and CCW rotations of the shuttling ring when one catalytic site has a blocking group, $k_{\rm attach,close}$ and $k_{\rm cleave,close}$ for addition and removal of a blocking group at the catalytic site nearest the shuttling ring, $k_{\rm attach,far}$ and $k_{\rm cleave,far}$ for the addition and removal rates from the catalytic site farthest from the shuttling

ring, and $k_{\rm sym}$ for rotations of the shuttling ring when no blocking groups are present. At each NESS simulation time step, the motor's configuration is classified as one of the eight states. If one makes a Markovian assumption, the rate for the transition from coarse-grained state A to state B is

$$k_{AB} = \frac{1}{p_{\rm ss}(A)} \frac{N_{AB}}{t_{\rm obs}}.$$
 (6)

Here $p_{\rm ss}(A)$ is the steady state probability of being in state A and N_{AB} is the number of transitions from A to B observed in time $t_{\rm obs}$. To extract the best rate estimate, transitions that are statistically equivalent by symmetry were combined, e.g. $k_{\rm cleave,far} = \frac{1}{t_{\rm tobs}} \frac{N_{21} + N_{34} + N_{56} + N_{87}}{p_{\rm ss}(2) + p_{\rm ss}(3) + p_{\rm ss}(5) + p_{\rm ss}(8)}$. Because we simulated a soft system with finite time steps, a transition between two disconnected states of Fig. 5 was very occasionally observed, but we neglected these transitions when constructing the rate model.

To analyze how the interplay between rates generates current, it is productive to decompose the eight-state rate model into four fundamental cycles (FC1 - FC4), shown in Fig. 5. Any possible cycle on the graph can be formed by a linear combination of this (non-unique) set of fundamental cycles. Only FC1 gates shuttling ring diffusion into directed motion at both catalytic sites. Traversing FC1 in the clockwise direction implies that the shuttling ring completes one CW cycle. A clockwise traversal around FC2 or FC3 similarly corresponds to CW shuttling ring cycling. However, the CW bias is only half that of FC1 because the shuttling ring direction is ambiguous when FC2 and FC3 pass through the unblocked states 4 and 6. The final cycle, FC4, is a futile cycle. Despite burning fuel to traverse FC4, no net cycles of the shuttling ring are generated.

An advantage of the fundamental cycle perspective is that the direction of the steady state currents follows from the ratio of rates around the closed fundamental cycles. For example, fundamental cycles FC2 and FC3 share the ratio

$$R = \frac{k_{\text{attach,far}}}{k_{\text{attach,close}}} \frac{k_{\text{cleave,close}}}{k_{\text{cleave,far}}} \frac{k_{\text{CW}}}{k_{\text{CCW}}}.$$
 (7)

We call the logarithm of this ratio the cycle affinity $\mathcal{A} = \log R$, and note that the steady state current around a FC must share the same sign as \mathcal{A} [53]. Because all four FCs have a cycle affinity that is a non-negative multiple of \mathcal{A} , the steady state current's sign is inherited from the sign of \mathcal{A} . Put more succinctly in terms of R, if R > 1 the shuttling ring will move clockwise and if R < 1 the shuttling ring will move counterclockwise.

Clockwise Directionality

We develop our understanding of the motor's clockwise motion by building off an equilibrium reference, for which

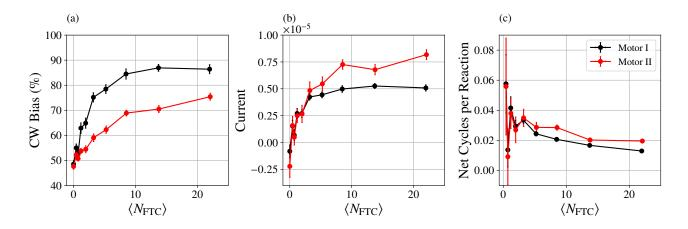


FIG. 3. Response of the motors to fuel, extracted from explicit NESS simulations. By adjusting $\mu'_{\rm FTC}$ from -1 to 1 in increments of 0.25 and holding fixed $\mu'_{\rm ETC} = \mu'_{\rm C} = -10$, the typical number of fuel molecules $\langle N_{\rm FTC} \rangle$ was tuned in accordance with Eq. (B10). The clockwise bias (a, Eq. (3)), current (b, Eq. (4)), and coupling (c, Eq. (5)) of the two motors were computed from 50 independent simulations of $t_{\rm obs} = 1 \times 10^6$ units of time each. Error bars represent the standard error across the 50 simulations.

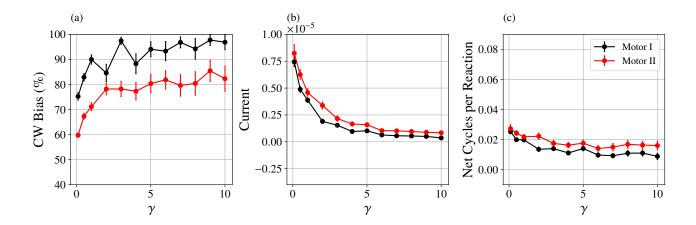


FIG. 4. Response of the motors to increased damping, extracted from explicit NESS simulations. For a fixed NESS with $\mu'_{\rm FTC}=0.5$, $\mu'_{\rm ETC}=\mu'_{\rm C}=-10$ (corresponding to $\langle N_{\rm FTC}\rangle=8.6$, $\langle N_{\rm ETC}\rangle=0.1$, and $\langle N_{\rm C}\rangle=0.9$), clockwise bias (a), current (b), and coupling (c) were simulated with variable friction coefficient γ . Reported data are the means and standard errors of 50 independent simulations of $t_{\rm obs}=1\times10^6$ units of time each. As the friction increases, the overall rates all decrease, causing some high-friction simulations to have no cycles in either direction. Those trials were excluded from the clockwise bias statistics, but were still included in the calculation of the current and the net cycles per catalyzed reaction.

R=1 is required by time-reversal symmetry. There are multiple ways to construct an equilibrium reference. For example, we could simulate the motor's equilibrium behavior when $\langle N_{\rm FTC} \rangle = \langle N_{\rm ETC} \rangle = \langle N_{\rm C} \rangle = 0$. With no C particles that equilibrium would confine the motor to states 4 and 6. Instead, we constructed a reference state with non-vanishing $\langle N_{\rm C} \rangle$ and with $\langle N_{\rm FTC} \rangle \approx \langle N_{\rm ETC} \rangle \approx 0$ by setting $\mu_{\rm C}' = -3$ and $\mu_{\rm FTC}' = \mu_{\rm ETC}' = -10$. In this way all eight coarse-grained states and all transitions are observed in the reference (which is essentially equivalent to an equilibrium simulation with a single $\mu_{\rm C}' = -3$ chemostat). We bias away from this equilibrium by increasing $\mu_{\rm FTC}'$.

Figure 6a shows that only the two rate constants regulating the blocking group attachment ($k_{\text{attach,close}}$ and $k_{\text{attach,far}}$) respond strongly to the fuel injection. Those attachment rates are functions of the fuel concentration, as one might expect from mass action kinetics when FTC reacts at the catalytic sites to leave behind C as a blocking group. Across the range of FTC concentration, the other five rates behave effectively the same as in the $\langle N_{\text{FTC}} \rangle = 0$ equilibrium reference state. To emphasize that the attachment rates are functions of fuel concentration, we adopt the notation $k_{\text{attach,*}}(\langle N_{\text{FTC}} \rangle)$. No argument is needed for the other rates because those rates are effectively independent of FTC concentration.

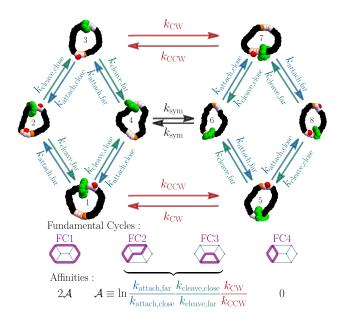


FIG. 5. Motor dynamics can be coarse grained onto an eightstate kinetic model based on the position of shuttling ring relative to the two binding sites and the presence or absence of at least one C particle blocking group at each catalytic site. Due to symmetries there are seven macroscopic rates in the system, labeled as transitions between certain states. The kinetic model decomposes into four fundamental cycles, shown in purple, with mean steady-state currents oriented in the same direction as the cycle affinities.

Since R = 1 at equilibrium,

$$\frac{k_{\text{attach,close}}(0)}{k_{\text{attach,far}}(0)} = \frac{k_{\text{cleave,close}}k_{\text{CW}}}{k_{\text{cleave,far}}k_{\text{CCW}}},$$
(8)

allowing the NESS R to be well approximated in terms of attachment rates alone:

$$R \approx R_{\rm approx} = \frac{k_{\rm attach,far}(\langle N_{\rm FTC} \rangle)}{k_{\rm attach,far}(0)} \frac{k_{\rm attach,close}(0)}{k_{\rm attach,close}(\langle N_{\rm FTC} \rangle)}. \tag{9}$$

Figure 6a shows that adding fuel increases attachment rates, both attachment near and far from the shuttling ring, but the speed-ups are not equal. Because $k_{\rm attach,far}$ increases more steeply than $k_{\rm attach,close},~R>1$ and current is clockwise. Our analysis of R shows that FC1, FC2, and FC3 all contribute to CW current, but FC1 contributes more strongly. By also monitoring the NESS population of the eight states (Fig. 6b), we show that increasing fuel takes population away from states 4 and 6, which lie on FC2 and FC3, but not FC1. The increase in CW bias with $\langle N_{\rm FTC} \rangle$ in Fig. 3a can be viewed as a consequence of the fully ratcheted FC1 cycle becoming dominant.

We note that even with our analysis, it is not obvious how the geometry of the design in Fig. 1 translates into the clockwise currents. The fuel-dependent attachment rates both increase with FTC concentration, and directionality is determined by which of those rates rises up more rapidly with added $N_{\rm FTC}$. We anticipate it will be possible to preserve the motor geometry and design changes to the motor's pairwise potential to yield R < 1 and counterclockwise cycles.

Thermodynamics

We have described an entirely kinetic analysis, but thermodynamics is linked to that kinetic via microscopic reversibility or local detailed balance. Each step of the NESS simulation is microscopically reversible—both the chemostat GCMC moves and the Langevin time steps, so the logarithmic ratio of probabilities of forward and reverse steps measures the increasing entropy of the ideal particle reservoirs. We caution, however, that such a close link between dynamics and thermodynamics hinges upon preserving the high-dimensional dynamics. When tracking all degrees of freedom, the pathway for converting from configuration x to y is identical to the timereversed pathway going from y to x. Upon coarse graining the configuration space (e.g. into the 8-state kinetic model) the link connecting forward and reversed rates to thermodynamics is more complicated. An effect of the coarse graining is that the typical path from coarsegrained state A to B may look nothing like the timereserved typical path from B to A. If the goal of the kinetic modeling is merely to explain directionality, the preceding analysis suffices, but if one wants to understand the thermodynamic cost of fueling the motor, it will be necessary to explicitly separate the different transition pathways, paying particular attention to the different reservoir contributions from each pathway.

To make this point more explicit, we elaborate upon the transitions between states 1 and 4, characterized simply by $k_{\rm cleave, close}$ and $k_{\rm attach, close}$ in Fig. 5. In equilibrium simulations with only C and no tetrahedral clusters, the pathways for cleavage and attachment are identical, but simulations with FTC reveal differing pathways for cleavage and attachment (see SI Movies 2 and 3). A minimal model to address the motor's thermodynamics must separate the pathways into the equilibrium-like process mediated by the C reservoir and an additional pathway mediated by the FTC and ETC reservoirs.

In light of these distinct mechanisms, we note that the previously described affinities $\mathcal A$ are cycle affinities of the Markov model and not thermodynamic affinities, which relate to the entropy produced by the motors. That physical entropy production can dramatically exceed the Markov model's entropy production when the rates of distinct pathways are clumped together as in Fig. 5. Consider, for example, Fig. 7, which illustrates a refinement to the kinetic model that resolves whether cleavage and attachment events were mediated by C alone $(k_{\rm attach}^{\rm C}$ and $k_{\rm cleave}^{\rm TC})$ or by a tetrahedral cluster reaction $(k_{\rm attach}^{\rm TC}$ and $k_{\rm cleave}^{\rm TC})$. The refinement does not alter the rate of shuttling ring current provided $k_{\rm attach}=k_{\rm attach}^{\rm C}+k_{\rm attach}^{\rm TC}$ and $k_{\rm cleave}=k_{\rm cleave}^{\rm C}+k_{\rm cleave}^{\rm TC}$. Though the current is insensi-

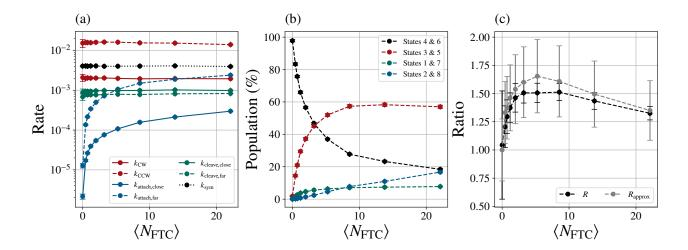


FIG. 6. (a) The transition rates of the eight-state model from Fig. 5 and (b) populations for each of the eight states for Motor II as a function of the average number of FTC present in the simulation $\langle N_{\rm FTC} \rangle$. (c) The ratio of rates $R(=e^A)$ and the approximate ratio from Eq. (9) as a function of FTC present. Data points show the average over 50 independent simulations of $t_{\rm obs} = 1 \times 10^6$ units of time each. FTC number is varied by changing $\mu'_{\rm FTC}$ from -10 and -1 to 1 in increments of 0.25.

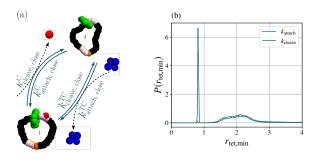


FIG. 7. Thermodynamic interpretation requires separation into pathways, distinguished by their interplay with the reservoirs. (a) The attachment rate $k_{\text{attach,close}}$ to pass from state 1 to 4 in Fig. 5 is a superposition of two rates: $k_{\text{attach,close}}^{\text{C}}$, the rate for a free C to bind, and $k_{\text{attach,close}}^{\text{TC}}$, the rate for a C to be extracted from an FTC to create a blocking group. Even though each pathway is microscopically reversible, typical transformations from 1 to 4 are not time-reversals of the typical transformations from 4 to 1. The former prefers the C pathway while the latter prefers TC. (b) The distinction between forward and reversed pathways is detected by recording the distance between the C blocking group and the nearest tetrahedral structure at the time of the attachment and cleavage transitions. Combining data from both "close" and "far" events with $\mu'_{\rm FTC} = 1$, $\mu'_{\rm C} = -3$, and $\mu'_{\rm ETC} = -10$, the distribution of distances $P(r_{\text{tet,min}})$ shows attachment events have a high probability of being mediated by a tetrahedral cluster evidenced by the large peak around the reaction distance of 0.8. By contrast, cleavage events have essentially no probability of happening via tetrahedral mediation.

tive to the refined model, the two Markov models produce entropy at different rates. The Fig. 7 Markov model includes additional cycles from state 1 to 4 and back via the other pathway, and the entropy production associ-

ated with those cycles is undetected by the Fig. 5 model. In other words, coarse graining yields a model that produces less entropy than the fine-grained model, a well-known effect of the data processing inequality that applies whether the coarse graining combines together microstates or pathways [54, 55]. It is therefore notable that our simulations give access to the reversibility of the trajectories in the full state space, not just the reversibility of some reduced Markov models. We anticipate that capability will be particularly beneficial for future studies of the thermodynamic performance.

Discussion

The models and methods presented here demonstrate a computational strategy to study how pairwise interactions give rise to dynamical function by simulating Langevin dynamics of a motor model simultaneously with GCMC chemostats. One can imagine carrying out similar, albeit vastly more expensive, simulations using more detailed, realistic models of chemical motors, but we highlight that our minimal toy model offers a tractable playground for exploring principles. It provides practical access to calculations of efficiency, accuracy, speed, and entropy production in a nontrivial particle-based model, opening the door to further explorations of thermodynamic and kinetic bounds [56, 57] that limit what sort of autonomous, steady-state motors can be designed. Those studies of the interplay between fluctuations and dissipation are commonly applied to abstract nonequilibrium Markov jump models without explicitly specifying the microscopic origin of the rates. We anticipate that the stochastic thermodynamics community will benefit from this toy model that enables an explicit connection between pair potentials and the mesoscopic transition rates. We also anticipate that our approach will be useful in testing proposed improvements to the motor's design [58].

More concretely, our work should aid in the design and implementation of autonomous mesoscale machines. While this work was inspired by a molecular scale motor [15], the pairwise potentials we use could more easily be built from mesoscale colloid constructions, where interactions between subunits can be tuned [59]. Significantly, we demonstrated that the motor maintains directional current in the overdamped regime, which is relevant to such colloidal diffusion. Although we do not expect our particular tetrahedral cluster fuel to be the most reasonable design on which to build an experimentally accessible mesoscale machine, we do hope the illustration and the methods will encourage more designs that will soon be experimentally realized.

METHODS

Model Details

We used a modified Lennard-Jones (LJ) potential for all non-bonded interactions between particles in the system. Unlike the standard WCA potential [60], which includes both r^{-12} and r^{-6} contributions in the repulsive regime, we modified pairwise LJ potentials by introducing separate control over the strength of the r^{-12} repulsive and r^{-6} attractive terms:

$$U_{\rm LJ}(\mathbf{r}_{ij}) = 4\epsilon_{\rm R,ij} \left(\frac{\sigma_{ij}}{|\mathbf{r}_{ij}|}\right)^{12} - 4\epsilon_{\rm A,ij} \left(\frac{\sigma_{ij}}{|\mathbf{r}_{ij}|}\right)^{6}, \quad (10)$$

where σ_{ij} is the average of the radii of particles i and j. The strength of the short-ranged repulsive interaction between particles i and j is tuned by $\epsilon_{R,ij}$, while that of the long-range attractive interaction is tuned by $\epsilon_{A,ij}$, as in [61]. All particles in the system are volume-excluding $(\epsilon_{R,ij} > 0)$, but only some pairwise interactions are attractive $(\epsilon_{A,ij} \geq 0)$. The full set of interaction parameters for each type of particle in the system is given in Table II of the Supplementary Information (SI).

The full tetrahedral cluster (FTC) fuel molecules are comprised of a four-particle tetrahedron bound along the edges (blue) and a free central particle (red), depicted in Fig. 1. The edges of the tetrahedron are held together with harmonic interactions that seek to minimize the distance \mathbf{r}_{ij} between particles i and j:

$$U_{\text{harmonic}}(\mathbf{r}_{ij}) = \frac{1}{2} k_{ij} \mathbf{r}_{ij}^2. \tag{11}$$

The values of the spring constants k_{ij} are found in SI Table II. The particle types of the tetrahedron are labeled as TET1, TET2, TET3, and TET4 while the central particle is called CENT. Pairwise interactions between all of these particle types are purely repulsive ($\epsilon_{A,ij}$ =

0). This ensures that FTC is a metastable, kinetically trapped state and it also ensures that FTC, ETC, and C do not aggregate in the simulation cell. Progress along the FTC \rightarrow ETC + C reaction pathway is tracked by measuring r, the distance between the C particle and the center of mass of the four tetrahedron particles. In non-dimensional units, the cluster is in the FTC state when $r \leq 0.25$, it is in the ETC + C state when $r \geq 0.8$, and it is in an intermediate transition regime, visited fleetingly, when 0.25 < r < 0.8.

The motor model is composed of two interlocked rings. A large ring consisting of $N_{\text{large}} = 30$ connected beads functions as a track for a smaller shuttling ring (green) with $N_{\rm shuttle} = 12$ beads to diffuse or "shuttle" around, as depicted in Fig. 1. The shuttling ring is made up of a single particle type, labeled SHUTTLE. The large ring is made up of three particle types: INERT particles that are purely volume excluding (black), BIND particles that have attractive interactions with the shuttling ring (orange), and catalytic particles (CAT1, CAT2, CAT3) that have attractive interactions with TET1, TET2, TET3, TET4, and CENT particles to facilitate the decomposition of FTC to ETC + C (white). The ring is arranged so that a three-particle catalytic site (CAT2-CAT1-CAT3 in clockwise order) is on the clockwise side of a singleparticle binding site, followed by a set of eleven inert particles before the binding/catalytic motif repeats on the opposite side of the large ring. The binding sites, located at large ring indices 0 and 15, are analogous to the fumaramide residues of the Wilson et al. motor [15]. The catalytic sites, located at large ring indices 1-3 and 16-18, are analogous to the hydroxy groups of the Wilson et al. motor. The attractive interaction between C (CENT) particles and the middle catalytic particle (CAT1) is particularly strong so as to hold the C particle near the catalytic site as a blocking group for the shuttling ring after a catalyzed reaction has occurred. Those blocking groups are especially effective at preventing the diffusion of the shuttling ring because C particles also have particularly strong repulsions with the shuttling ring particles (SHUTTLE).

The rings have intramolecular interactions similar to those used for coarse-grained polymer models where bond and angle potentials maintain geometry and the modified Lennard-Jones potential of Eq. (10) serves to include volume exclusion. The bonded interactions between adjacent beads in the motor rings is given by a finitely extensible nonlinear spring (FENE) potential:

$$U_{\text{FENE}}(\mathbf{r}_{ij}) = -\frac{1}{2} k_{\text{F},ij} \mathbf{r}_{ij}^2 \log \left[1 - \left(\frac{|\mathbf{r}_{ij}|}{r_{\text{max},ij}} \right)^2 \right]. \quad (12)$$

Here \mathbf{r}_{ij} is the displacement vector between particles i and j, $k_{\mathrm{F},ij}$ is the FENE force constant, and $r_{\mathrm{max},ij}$ is the maximum extension between the particle pair. Groups of three adjacent ring particles also have angular interactions to maintain the overall circular geometry of the

ring:

$$U_{\text{angle}}(\theta_{ijk}) = \frac{1}{2} k_{\text{A},ijk} \left(\theta_{ijk} - \theta_{0,ijk}\right)^2, \qquad (13)$$

where i is the index of the middle particle of the three adjacent i, j, and k particles, $k_{\mathrm{A},ijk}$ is the angular force constant, θ_{ijk} is the angle formed by the three particles, and $\theta_{0,ijk}$ is the equilibrium angle. For the shuttling ring $\theta_{0,ijk} = \pi \left(1 - \frac{2}{N_{\mathrm{shuttle}}}\right)$ and for the large ring $\theta_{0,ijk} = \pi \left(1 - \frac{2}{N_{\mathrm{large}}}\right)$. The bond and angle parameters as well as the modified LJ parameters for all of the motor particles are found in SI Table II and Table III. The shuttling ring and large ring are placed in an interlocked configuration. No bonded (FENE or angular) interactions connect the two rings as they can be held in an interlocked state through the volume exclusion of the LJ interaction alone. The shuttling ring is therefore free to diffuse around the large ring.

Method Details

To propagate the system dynamics forward in time we solve Eq. (2) numerically with a time step of $\Delta t = 5 \times 10^{-3}$ for some number of time steps N_{steps} using the integrator of Athènes and Adjanor [62]:

$$\mathbf{p}_{i}^{j+\frac{1}{2}} = \mathbf{p}_{i}^{j} e^{-\frac{\gamma \Delta t}{2m_{i}}} + \mathbf{f}_{i}^{j} \frac{\Delta t}{2} + \boldsymbol{\eta}_{i}^{j+\frac{1}{2}}$$

$$\mathbf{r}_{i}^{j+1} = \mathbf{r}_{i}^{j} + \mathbf{p}_{i}^{j+\frac{1}{2}} \frac{\Delta t}{m_{i}}$$

$$\mathbf{p}_{i}^{j+1} = \left[\mathbf{p}_{i}^{j+\frac{1}{2}} + \mathbf{f}_{i}^{j+1} \frac{\Delta t}{2}\right] e^{-\frac{\gamma \Delta t}{2m_{i}}} + \boldsymbol{\eta}_{i}^{j+1}, \qquad (14)$$

where $\mathbf{f}_i = -\nabla U(\mathbf{r}_i)$ is the force on particle $i, \mathbf{r}_i^j \equiv$ $\mathbf{r}_i(j\Delta t)$ is the position of particle i at time $j\Delta t$, $\mathbf{p}_{i}^{j} \equiv \mathbf{p}_{i}(j\Delta t)$ is the momentum of particle i at time $j\Delta t$, and each η_i is a random vector with components drawn from a zero-mean Gaussian with variance $m_i(1 \exp(-\gamma \Delta t/m_i))k_{\rm B}T$. Other choices of numerical integrator are possible [63]. We performed all simulations in non-dimensional form with characteristic length given by the LJ radius of an INERT particle, characteristic energy given by the repulsive strength of the INERT-INERT interaction, and characteristic mass given by the mass of an INERT particle. All of these values were then set to unity, i.e. $(\sigma_{\text{INERT}} = 1, m_{\text{INERT}} = 1, \epsilon_{\text{R,INERT-INERT}} =$ 1), respectively. All other particle masses were also set to unity, and the only particles with non-unit radii were CENT particles with $\sigma_{\text{CENT}} = 0.45$. We report data for simulations with $k_{\rm B}T=0.5$ and with $\gamma=0.5$, except where otherwise noted. For completeness, the full set of particle mass and size parameters are given in SI Table I.

We performed a grand canonical Monte Carlo (GCMC) move every 100 Langevin time steps in order to maintain the system at a steady state concentration of FTC, ETC,

and C. The GCMC moves were conditionally accepted so the chemostatted region of space would target the grand canonical distribution

$$P(\mathbf{r}, \mathbf{p}) = \frac{1}{\Xi} \frac{e^{\beta \mu_{\text{FTC}} N_{\text{FTC}} + \beta \mu_{\text{ETC}} N_{\text{ETC}} + \beta \mu_{\text{C}} N_{\text{C}} - \beta H(\mathbf{r}, \mathbf{p})}}{N_{\text{FTC}}! N_{\text{ETC}}! N_{\text{C}}!},$$
(15)

where \mathbf{r} and \mathbf{p} are vectors of fluctuating length containing the coordinates for each copy of each species and Ξ is the grand canonical partition function. The number of copies of each species $(N_{\mathrm{FTC}}, N_{\mathrm{ETC}}, \text{ and } N_{\mathrm{C}})$ can be viewed as functions of \mathbf{r} and \mathbf{p} , as can the total energy $H(\mathbf{r}, \mathbf{p})$, the kinetic energy $K(\mathbf{p})$, and the potential energy $U(\mathbf{r})$. Though we are ultimately interested in unlabeled particles, it is simplest to utilize unphysical labels for accounting purposes. Marginalizing over all equally probable permutations of labels gives the density for unlabeled particles, which lacks the denominator of Eq. (15).

In practice, the GCMC method described here differs slightly from a standard implementation [18] since two of the species coupled to external chemical potentials (FTC and ETC) have internal degrees of freedom. Each GCMC chemostat move begins by uniformly selecting which of the three species to act on and whether to add or remove that species. The chemostat only acts on the outer volume of Fig. 1, and all copies of the chosen species occupying that outer volume are equally likely to be removed in the generated trial move. In the usual Metropolis manner, that trial removal of the copy of species i is conditionally accepted with probability

$$P_{i \text{ removal}}^{\text{acc}}(\mathbf{r}, \mathbf{p} \to \mathbf{r}', \mathbf{p}') = \min \left[1, N_{i}(\mathbf{r}) e^{-\beta(U(\mathbf{r}') - U(\mathbf{r}) + U_{i}^{0})} e^{-\beta(\mu_{i} - A_{i}^{0})} \right],$$
(16)

where U^0 is the potential energy of the removed cluster, Z_i^0 is the canonical partition function for a single i cluster in a box of volume V_0 , and $A_i^0 = -k_{\rm B}T\log Z_i^0$ is the associated free energy. In this work, we have operated in terms of the shifted chemical potential $\mu_i' \equiv \mu_i - A_i^0$ so the conditional acceptance probability was computed without needing to explicitly compute A_i^0 for the different cluster types. We tune these shifted chemical potentials from $\mu' = -10$ on the low end to $\mu' = 1$ on the high end.

The moves that add a cluster are more complicated because we must first generate a configuration of the cluster [40]. We used Monte Carlo to pre-generate an equilibrium ensemble of 10,000 configurations of a single FTC cluster and of a single ETC cluster. An addition move first uniformly selects one of those Boltzmann-distributed configurations (a step which is moot when adding C). This configuration is randomly rotated in space then randomly inserted into the chemostatted volume. Velocities for the new particles are sampled from the Boltzmann distribution to complete the generation of trial coordinates ${\bf r'}$ and ${\bf p'}$. Analogous to the removal moves, the

addition is conditionally accepted with probability

$$P_{i \text{ addition}}^{\text{acc}}(\mathbf{r}, \mathbf{p} \to \mathbf{r}', \mathbf{p}') = \min \left[1, \frac{1}{N_{i}(\mathbf{r}')} e^{-\beta(U(\mathbf{r}') - U(\mathbf{r}) - U_{i}^{0})} e^{\beta(\mu_{i} - A_{i}^{0})} \right].$$

$$(17)$$

One confirmation that all three chemostats simultaneously function as desired is the demonstration of ideality in the dilute limit, discussed further in the SI.

These GCMC moves only occur in the space between the inner and outer simulation boxes, depicted in Fig. 1. Our simulation boxes were concentric cubes with inner side length $L_{\rm inner}=30$ and an outer cube of side length $L_{\rm outer}=34$. The motor itself is confined to the inner simulation box so that its dynamics are not directly perturbed by abrupt GCMC insertions and deletions. The motor is confined to the inner box with a LJ wall potential:

$$U_{\text{wall}}(\mathbf{r}_i) = 4\epsilon_{\text{wall}} \sum_{\alpha = x, y, z} \left[\left(\frac{\sigma_{\text{wall}}}{r_{\alpha, i} - \frac{1}{2}L_{\text{inner}}} \right)^{12} + \left(\frac{\sigma_{\text{wall}}}{r_{\alpha, i} + \frac{1}{2}L_{\text{inner}}} \right)^{12} \right],$$
(18)

where $\mathbf{r}_i = (r_{x,i}, r_{y,i}, r_{z,i})$ is the position of the i^{th} motor

particle and both boxes are centered at the origin. We set $\epsilon_{\text{wall}} = 1$ and $\sigma_{\text{wall}} = 1$. Particles of the FTC, ETC, and C molecules do not experience this wall potential and move freely between the inner and outer boxes. These species are also free to pass through the periodic boundaries of the outer box, which we implemented using the minimum image convention [18].

DATA AVAILABILITY

The datasets generated and analyzed during the current study will be available in a Zenodo.com repository with a persistent DOI.

CODE AVAILABILITY

The source code and analysis scripts used in the current study will be available in a Zenodo.com repository with a persistent DOI.

ACKNOWLEDGMENTS

The authors gratefully acknowledge productive conversations with Hadrien Vroylandt, Geyao Gu, and Rueih-Sheng Fu. Research reported in this publication was supported in part by the International Institute for Nanotechnology at Northwestern University.

- J. Howard, A. Hudspeth, and R. Vale, Nature 342, 154 (1989).
- [2] J. T. Finer, R. M. Simmons, and J. A. Spudich, Nature 368, 113 (1994).
- [3] A. I. Brown and D. A. Sivak, Chemical Reviews 120, 434 (2019).
- [4] A. B. Kolomeisky and M. E. Fisher, Annu. Rev. Phys. Chem. 58, 675 (2007).
- [5] F. Jülicher, A. Ajdari, and J. Prost, Reviews of Modern Physics 69, 1269 (1997).
- [6] M. L. Mugnai, C. Hyeon, M. Hinczewski, and D. Thirumalai, Reviews of Modern Physics 92, 025001 (2020).
- [7] R. D. Vale, T. Funatsu, D. W. Pierce, L. Romberg, Y. Harada, and T. Yanagida, Nature 380, 451 (1996).
- [8] K. S. Thorn, J. A. Ubersax, and R. D. Vale, The Journal of Cell Biology 151, 1093 (2000).
- [9] M. F. Engelke, M. Winding, Y. Yue, S. Shastry, F. Teloni, S. Reddy, T. L. Blasius, P. Soppina, W. O. Hancock, V. I. Gelfand, et al., Nature Communications 7, 1 (2016).
- [10] Z. Bryant, D. Altman, and J. A. Spudich, Proceedings of the National Academy of Sciences 104, 772 (2007).
- [11] J.-C. Liao, M. W. Elting, S. L. Delp, J. A. Spudich, and Z. Bryant, Journal of Molecular Biology 392, 862 (2009).
- [12] T. R. Kelly, I. Tellitu, and J. P. Sestelo, Angewandte Chemie International Edition 36, 1866 (1997).

- [13] T. R. Kelly, H. De Silva, and R. A. Silva, Nature 401, 150 (1999).
- [14] T. R. Kelly, X. Cai, F. Damkaci, S. B. Panicker, B. Tu, S. M. Bushell, I. Cornella, M. J. Piggott, R. Salives, M. Cavero, et al., Journal of the American Chemical Society 129, 376 (2007).
- [15] M. R. Wilson, J. Solà, A. Carlone, S. M. Goldup, N. Lebrasseur, and D. A. Leigh, Nature 534, 235 (2016).
- [16] C. Bustamante, D. Keller, and G. Oster, Accounts of Chemical Research 34, 412 (2001).
- [17] R. D. Astumian, Physical Chemistry Chemical Physics 9, 5067 (2007).
- [18] D. Frenkel and B. Smit, Understanding Molecular Simulation: From Algorithms to Applications, Vol. 1 (Elsevier, 2001).
- [19] R. D. Astumian, Nature Nanotechnology 7, 684 (2012).
- [20] X. Fang, K. Kruse, T. Lu, and J. Wang, Reviews of Modern Physics 91, 045004 (2019).
- [21] N. Koga and S. Takada, Proceedings of the National Academy of Sciences 103, 5367 (2006).
- [22] Y. Isaka, T. Ekimoto, Y. Kokabu, I. Yamato, T. Murata, and M. Ikeguchi, Biophysical Journal 112, 911 (2017).
- [23] Y. Togashi and A. S. Mikhailov, Proceedings of the National Academy of Sciences 104, 8697 (2007).
- [24] M.-J. Huang, R. Kapral, A. S. Mikhailov, and H.-Y. Chen, The Journal of Chemical Physics 138, 05B613_1

- (2013).
- [25] A. Cressman, Y. Togashi, A. S. Mikhailov, and R. Kapral, Physical Review E 77, 050901 (2008).
- [26] S. Mukherjee, R. Alhadeff, and A. Warshel, Proceedings of the National Academy of Sciences 114, 2259 (2017).
- [27] E. M. Craig and H. Linke, Proceedings of the National Academy of Sciences 106, 18261 (2009).
- [28] K.-i. Okazaki and G. Hummer, Proceedings of the National Academy of Sciences 110, 16468 (2013).
- [29] K.-i. Okazaki and G. Hummer, Proceedings of the National Academy of Sciences 112, 10720 (2015).
- [30] K. Nam, J. Pu, and M. Karplus, Proceedings of the National Academy of Sciences 111, 17851 (2014).
- [31] J. Pu and M. Karplus, Proceedings of the National Academy of Sciences 105, 1192 (2008).
- [32] L. Dai, H. Flechsig, and J. Yu, Biophysical Journal 113, 1440 (2017).
- [33] J. Czub, M. Wieczór, B. Prokopowicz, and H. Grubmüller, Journal of the American Chemical Society 139, 4025 (2017).
- [34] S. Amano, S. Borsley, D. A. Leigh, and Z. Sun, Nature Nanotechnology, 1 (2021).
- [35] Q. Xiao, Y. Chen, T. Bereau, and Y. Shi, Chemical Physics Letters 659, 6 (2016).
- [36] G. Rückner and R. Kapral, Physical Review Letters 98, 150603 (2007).
- [37] Y.-G. Tao and R. Kapral, The Journal of Chemical Physics 128, 164518 (2008).
- [38] L. F. Valadares, Y.-G. Tao, N. S. Zacharia, V. Kitaev, F. Galembeck, R. Kapral, and G. A. Ozin, Small 6, 565 (2010).
- [39] P. H. Colberg, S. Y. Reigh, B. Robertson, and R. Kapral, Accounts of Chemical Research 47, 3504 (2014).
- [40] S. Chempath, L. A. Clark, and R. Q. Snurr, The Journal of Chemical Physics 118, 7635 (2003).
- [41] E. Gerritsma and P. Gaspard, Biophysical Reviews and Letters 5, 163 (2010).
- [42] U. Seifert, The European Physical Journal E **34**, 1 (2011).
- [43] B. Altaner, A. Wachtel, and J. Vollmer, Physical Review E 92, 042133 (2015).
- [44] H. Noji, R. Yasuda, M. Yoshida, and K. Kinosita, Nature 386, 299 (1997).
- [45] R. Yasuda, H. Noji, K. Kinosita Jr, and M. Yoshida, Cell 93, 1117 (1998).
- [46] P. M. Hoffmann, Reports on Progress in Physics 79, 032601 (2016).
- [47] R. D. Astumian, Nature Nanotechnology 11, 582 (2016).
- [48] Y. Qiu, Y. Feng, Q.-H. Guo, R. D. Astumian, and J. F. Stoddart, Chem 6, 1952 (2020).
- [49] R. D. Astumian, Science **276**, 917 (1997).
- [50] M. Bier and R. D. Astumian, Bioelectrochemistry and Bioenergetics 39, 67 (1996).
- [51] R. D. Astumian, S. Mukherjee, and A. Warshel, ChemPhysChem 17, 1719 (2016).
- [52] A. Gupta, L. A. Clark, and R. Q. Snurr, Langmuir 16, 3910 (2000).
- [53] J. W. Biddle and J. Gunawardena, Physical Review E 101, 062125 (2020).
- [54] A. Puglisi, S. Pigolotti, L. Rondoni, and A. Vulpiani, Journal of Statistical Mechanics: Theory and Experiment 2010, P05015 (2010).
- [55] M. Esposito, Physical Review E 85, 041125 (2012).

- [56] J. M. Horowitz and T. R. Gingrich, Nature Physics 16, 15 (2020).
- [57] I. Di Terlizzi and M. Baiesi, Journal of Physics A: Mathematical and Theoretical 52, 02LT03 (2018).
- [58] S. Amano, M. Esposito, E. Kreidt, D. A. Leigh, E. Penocchio, and B. M. Roberts, ChemRxiv (2021), 10.33774/chemrxiv-2021-60k1r.
- [59] S. Angioletti-Uberti, B. M. Mognetti, and D. Frenkel, Physical Chemistry Chemical Physics 18, 6373 (2016).
- [60] J. D. Weeks, D. Chandler, and H. C. Andersen, The Journal of Chemical Physics 54, 5237 (1971).
- [61] A. Albaugh and T. R. Gingrich, The Journal of Chemical Physics 153, 204102 (2020).
- [62] M. Athenes and G. Adjanor, The Journal of Chemical Physics 129, 024116 (2008).
- [63] J. Fass, D. A. Sivak, G. E. Crooks, K. A. Beauchamp, B. Leimkuhler, and J. D. Chodera, Entropy 20, 318 (2018).

SUPPLEMENTARY INFORMATION (SI)

Appendix A: Movie Files

Three SI Movies depict representative simulations. All movies show dynamics at moderate fuel concentration with $\mu'_{\rm FTC} = 0.5$, $\mu'_{\rm ETC} = -10$, and $\mu'_{\rm C} = -10$. The file Motor_Operation.gif shows the dynamics of the full simulation cell with frames taken every 50,000 time steps. The movie shows a clear preference for clockwise motion over counterclockwise motion. The Cleave_Close.gif and Attach_Close.gif movie files show representative pathways for the $k_{\rm cleave,close}$ and $k_{\rm attach,close}$ pathways, respectively. In these movies each frame represents 50 individual time steps. The cleave pathway shows that the transitions happens with a simple unbinding of a red C particle from the close catalytic site. The attach pathway shows a transition that occurs as an FTC cluster decomposes into ETC and C at the catalytic site, leaving behind a C particle as a blocking group. These two pathways are not time-reverses of each other.

In all movie files we translated and rotated the system configuration in each frame to give a clear view of the shuttling ring's relative motion in the frame of a stationary large ring. We first translated the motor's center of mass to the center of the frame and then performed rotations so that the (orange) binding sites were at, approximately, the 12 o'clock and 6 o'clock positions and the large ring was in a plane approximately perpendicular to the observer.

Appendix B: Grand Canonical Monte Carlo Details

To target the grand Canonical distribution of Eq. (15), GCMC trial moves are attempted throughout a volume V_0 . Using the Metropolis criterion, the probability of inserting an additional i molecule and accepting this trial

move is

$$P_{i \text{ addition}}^{\text{acc}}(\mathbf{r}, \mathbf{p} \to \mathbf{r}', \mathbf{p}') = \min \left[1, \frac{P(\mathbf{r}', \mathbf{p}')}{P(\mathbf{r}, \mathbf{p})} \frac{P_{i \text{ removal}}^{\text{gen}}(\mathbf{r}', \mathbf{p}' \to \mathbf{r}, \mathbf{p})}{P_{i \text{ addition}}^{\text{gen}}(\mathbf{r}, \mathbf{p} \to \mathbf{r}', \mathbf{p}')} \right]$$
(B1)

where P^{gen} is the probability of generating such a trial move. Here we adopt a notation where \mathbf{r}, \mathbf{p} denotes the positions and momenta, respectively, of all particles in the initial system with $N_i(\mathbf{r})$ molecules of species i (where i can be FTC, ETC, or C). The trial move inserts an additional molecule of i and the positions and momenta of all particles in this configuration is given by \mathbf{r}', \mathbf{p}' . The probabilities $P(\mathbf{r}, \mathbf{p})$ and $P(\mathbf{r}', \mathbf{p}')$ are given by the grand canonical distribution, Eq. (15).

The probability of generating the insertion move is the probability of uniformly selecting that the next move would be an insertion of species i times the probability that the inserted species will be given a particular label in the list of i species times the Boltzmann probability of the inserted molecular configuration:

$$P_{i \text{ insertion}}^{\text{gen}}(\mathbf{r}, \mathbf{p} \to \mathbf{r}', \mathbf{p}') = \frac{1}{6} \frac{1}{N_i(\mathbf{r}')} \frac{e^{-\beta H(\mathbf{r}^0, \mathbf{p}^0)}}{Z_i^0}. \quad (B2)$$

Here \mathbf{r}^0 and \mathbf{p}^0 are the positions and momenta, respectively, of only the inserted molecule's particles. The trial configuration \mathbf{r}', \mathbf{p}' is then $\mathbf{r}, \mathbf{p} \cup \mathbf{r}^0, \mathbf{p}^0$ The total energy $H(\mathbf{r}^0, \mathbf{p}^0)$ is the internal energy of the inserted molecule if it were in isolation, with a normalizing partition function Z_i^0 for the single species i in a volume equal to the volume available for GCMC moves, V_0 :

$$Z_i^0 = \frac{1}{h^{3n_i}} \int d\mathbf{p}^0 \int_{V_0} d\mathbf{r}^0 e^{-\beta H(\mathbf{r}^0, \mathbf{p}^0)}.$$
 (B3)

Here h is Planck's constant and n_i is the number of particles in species i. Practically, to achieve configurations to insert that come from this Boltzmann ensemble we first pre-sample the FTC and ETC species with standard Markov chain Monte Carlo to build a library of configurations [40]. We then uniformly choose a configuration from this library, rotate that configuration into a uniformly sampled orientation, then place it inside the volume V_0 at a uniformly sampled location. Random velocities for all the inserted particles are sampled from the Boltzmann ensemble independently of the positions. The library generation and random rotation are not necessary for the C species since it is a single spherically symmetrical particle with no internal potential energy.

The probability of generating the reversal of the insertion move is simply the probability of choosing to remove a species i particle times the probability of selecting the particular one of the $N_i(\mathbf{r}')$ particles to delete:

$$P_{i \text{ removal}}^{\text{gen}}(\mathbf{r}', \mathbf{p}' \to \mathbf{r}, \mathbf{p}) = \frac{1}{6} \frac{1}{N_i(\mathbf{r}')}.$$
 (B4)

Substituting Eq. (15), Eq. (B2), and Eq. (B4) into Eq. (B1) yields

$$P_{i \text{ addition}}^{\text{acc}}(\mathbf{r}, \mathbf{p} \to \mathbf{r}', \mathbf{p}') = \min \left[1, \frac{1}{N_{i}(\mathbf{r}')} e^{-\beta [H(\mathbf{r}', \mathbf{p}') - H(\mathbf{r}, \mathbf{p}) - H(\mathbf{r}^{0}, \mathbf{p}^{0})]} e^{\beta \mu_{i}} Z_{i}^{0} \right].$$
(B5)

Recognizing that kinetic energy is purely additive across particles, $K(\mathbf{p}') = K(\mathbf{p}) + K(\mathbf{p}^0)$, and that $A_i^0 = -\log Z_i^0/\beta$ is the Helmholtz free energy of a single molecule of species i in volume V_0 , we can simplify even further, yielding

$$P_{i \text{ addition}}^{\text{acc}}(\mathbf{r}, \mathbf{p} \to \mathbf{r}', \mathbf{p}')$$

$$= \min \left[1, \frac{1}{N_i(\mathbf{r}')} e^{-\beta [U(\mathbf{r}') - U(\mathbf{r}) - U(\mathbf{r}^0)]} e^{\beta \mu_i'} \right].$$
(B6)

In a similar way, the acceptance probability of a trial move that removes a molecule of species i is given as

$$P_{i \text{ removal}}^{\text{acc}}(\mathbf{r}, \mathbf{p} \to \mathbf{r}', \mathbf{p}')$$

$$= \min \left[1, N_i(\mathbf{r}) e^{-\beta [U(\mathbf{r}') - U(\mathbf{r}) + U(\mathbf{r}^0)]} e^{-\beta \mu_i'} \right].$$
(B7)

In both cases we introduce the definition $\mu'_i \equiv \mu_i - A_i^0$ as a modified chemical potential that is the true external chemical potential less the free energy of the corresponding species at a reference state with a single molecule in volume V_0 and inverse temperature β . We need not calculate this free energy and can instead use μ'_i as the "knob" to turn to adjust the concentration of species in the simulation box. We would only need to calculate A_i^0 if we wanted to know the true absolute external chemical potential μ_i . As μ'_i becomes larger the concentration of species in the simulation box will increase and as μ'_i decreases the concentration will decrease. By setting a high chemical potential for FTC and low chemical potential for ETC and C, we can set up a NESS as the FTC decomposes to form ETC and C.

To summarize, a GCMC step begins by uniformly selecting one of six trial moves-insertion or deletion of either FTC, ETC, or C. If an insertion move for FTC or ETC is selected then a configuration of the species is selected from a pre-sampled equilibrium Boltzmann library [40]. This configuration is then randomly rotated. In our case we generated libraries of 10,000 samples for FTC and ETC using standard Markov chain Monte Carlo. The inserted molecule is then uniformly placed in the insertion volume V_0 and velocities are assigned according the Boltzmann distribution. If a deletion move is selected, a uniformly chosen molecule of the species is removed from the simulation box (if there is at least one molecule of the species present). In either case, the trial move is conditionally accepted, with rejected moves returning the system to its original state. Following the GCMC move, the system undergoes Langevin dynamics for a certain number of time steps until the GCMC procedure is repeated. With Langevin time step $\Delta t = 0.005$

we find that 100 time steps between GCMC trial moves is sufficient to maintain equilibrated chemostats.

The relationship between the external chemical potential μ_i and the internal composition is given by

$$\mu_i = A_i^0 + \frac{1}{\beta} \log \gamma_i \frac{\langle C_i \rangle}{C_i^0}.$$
 (B8)

With concentration $C_i = N_i/V$ and reference concentration $C_i^0 = 1/V$, the relationship between chemical potential and composition simplifies to

$$\mu_i' = \frac{1}{\beta} \log \gamma_i \langle N_i \rangle. \tag{B9}$$

The non-ideality of the solution is packaged into the activity coefficient γ_i . At low concentrations, the solution is ideal ($\gamma_i \approx 1$) because intermolecular interactions are small. As the concentration becomes larger these interactions start to dominate and the relationship between chemical potential and composition becomes non-ideal.

With our motor system we only perform GCMC moves in an outer volume, away from the motor (see Fig. 1). This is done to keep the natural dynamics of the motor unperturbed by abrupt insertions and deletions. If the volume where GCMC moves take place is V_0 , which is less than the total simulation volume accessible to the molecules V, and we assume that the diffusion of the molecules is fast relative their reaction (the diffusive Damköhler number is low) then the composition is given as

$$\langle N_i \rangle = \frac{V}{V_0} \frac{1}{\gamma_i} e^{\beta \mu_i'}.$$
 (B10)

From Fig. 10b we see that as $\mu'_{\rm FTC}$ is cycled between high and low values the composition of FTC reaches a new steady state very quickly, justifying this assumption. The simulations in Fig. 10 switched between $\mu'_{\rm FTC} = 0.5$ (shaded) and $\mu'_{\rm FTC} = -10$ (unshaded). The total volume $V = L^3_{\rm outer}$ with $L_{\rm outer} = 34$ with the GCMC volume $V_0 = L^3_{\rm outer} - L^3_{\rm inner}$ and $L_{\rm outer} = 30$. The inverse temperature β is 2. Assuming a dilute solution $\gamma_i \approx 1$ then from Eq. (B10) we would expect $\langle N_{\rm FTC} \rangle \approx 8.7$ for the shaded areas of Fig. 10a and $\langle N_{\rm FTC} \rangle \approx 0$ for the unshaded areas, matching the simulation data well. Thus, at these simulation parameters, the assumptions of ideal solution and low Damköhler number are justified.

As further proof that we can assume our simulations are ideal solutions and that the GCMC chemostats are working as expected, we performed tests where the entire simulation volume was available for GCMC moves and no motor was present. Those simulations were carried out with the full potential and also with non-interacting simulations where intermolecular interactions between different molecules in the simulation were not included. The ideal, non-interacting system allows for direct comparison with Eq. (B9) when $\gamma_i=1$. As shown in Fig. 8, non-ideality begins to emerge around $\mu_i'=1$.

Appendix C: Control Simulations

1. Chemostat Concentrations

The results of Figs. 3a and b demonstrate clear net clockwise cycling of the motor. In Fig 3a for moderate numbers of FTC in the simulation box $(\langle N_{\rm FTC} \rangle \approx 2-8)$ both type I and II motors show significantly increased accuracy above the equilibrium random cycling of 50%. Both motors also show significantly increased current in this range of FTC concentration compared to an equilibrium expectation value of 0. To demonstrate that this net directional cycling is coupled to the reaction of FTC to ETC and C we carried out a series of control simulations where the external chemical potential of FTC was set to -10, low enough that no FTC is expected to appear in the simulation. The concentrations of other species were then varied to determine their effect on the motor. We varied the concentrations of ETC, C, and a variant of FTC where the free central particle was no longer free. but constrained with a FENE spring to the center of the tetrahedron. For all intents and purposes, this constrained FTC (FTC(c)) is almost identical to FTC, but cannot react to form ETC and C. The form of the constraint for FTC(c) was

$$U_{\text{FENE}}(\mathbf{r}_c) = -\frac{1}{2} k_{\text{constraint}} \mathbf{r}_c^2 \log \left[1 - \left(\frac{|\mathbf{r}_c|}{r_{\text{max,c}}} \right)^2 \right], \tag{C1}$$

where \mathbf{r}_c is the vector between the central particle and the center of mass of the four tetrahedron particles, $k_{\text{constrain}} = 120$, and the maximum extension, $r_{\text{max,c}}$ is given as the maximum distance that defines the FTC molecule as being in a reactant state, 0.25 in our case.

The results of these control simulations, presented in Fig. 9, show that for all three species ETC, C, and FTC(c) there is no deviation from an accuracy of 50% and a current of 0. In other words, these simulations are all equilibrium simulations as the decomposition of FTC and its replenishment through the external chemical potential is required to establish a nonequilibrium steady state.

2. Chemostat Timescales

To realize current, it was necessary that the chemostats behave sufficiently quickly that NESS concentrations of FTC, ETC, and C could be achieved significantly faster than the timescale for shuttling ring diffusion. We check that this criterion is satisfied by periodically switching from $\mu'_{\rm FTC}=0.5$ to $\mu'_{\rm FTC}=-10$, while holding fixed $\mu'_{\rm ETC}=\mu'_{\rm C}=-10$. The responses to this time-periodic perturbation, plotted in Fig. 10, show that the FTC and ETC concentrations relax to their NESS values very rapidly, while the concentration of C relaxes more gradually due to its attractive interactions with the catalytic

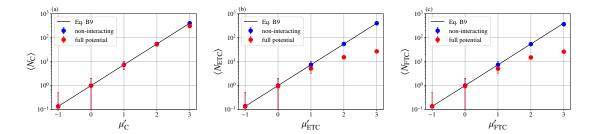


FIG. 8. Average number of species in the simulation volume of (a) C as a function of $\mu'_{\rm C}$ with $\mu'_{\rm FTC} = \mu'_{\rm ETC} = -10$, (b) ETC as a function of $\mu'_{\rm ETC}$ with $\mu'_{\rm FTC} = \mu'_{\rm C} = -10$, and (c) FTC as a function of $\mu'_{\rm FTC}$ with $\mu'_{\rm ETC} = \mu'_{\rm C} = -10$. Simulation data is given for the full potential (red) as well as a non-interacting potential (blue) where intermolecular interactions are turned off. The expected relationship between μ'_{i} and expected average number of species for an ideal solution ($\gamma_{i} = 1$) given by Eq. (B9) is given for reference (black). Simulations use a time step of $\Delta t = 0.005$ with 100 Langevin dynamics time steps between attempted GCMC moves. No motors are present in the simulations and GCMC moves can occur throughout the entire volume.

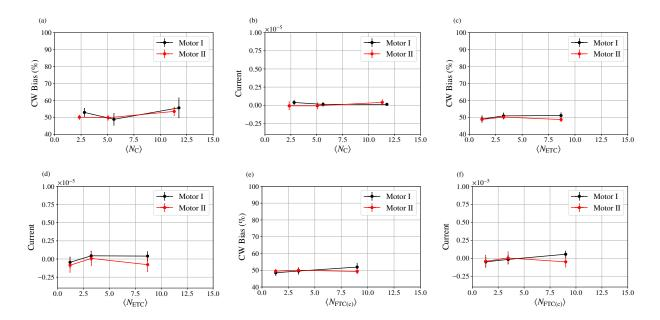


FIG. 9. Control simulations where the concentration of C (a, b), ETC (c, d), and FTC(c) (e, f) are varied and clockwise bias (a, c, e, Eq. (3)) and current (b, d, f, Eq. (4)) are examined. Each data point represents 50 independent simulations of 1×10^6 units of time with the mean plotted and the standard error of the mean represented by error bars.

sites of the motor. Even with this slower relaxation, that central particle equilibrates much faster than the typical timescale to complete cycles. Consequently, the periodically driven motor alternates between regimes of fueled directed motion (shaded) and unfueled equilibrium diffusion (unshaded). When FTC is present the motor has a clear bias toward the CW direction and when FTC is not present the motor reverts to unbiased diffusion where it can cycle CW or CCW with equal probability, resulting in no net current.

Appendix D: Forcefield Parameters

The model consists of 11 different particle types: the two binding sites on the large ring (BIND), 22 inert sites on the large ring (INERT), six catalytic sites (2 each of CAT1, CAT2, and CAT3), 12 sites around the shuttling ring (SHUTTLE), four different types of particles on the vertices of the tetrahedra (TET1, TET2, TET3, and TET4), and the central particle (CENT). The forcefield is fully defined by the masses and radii of these particles (Table I), the pairwise interactions (Table II), and the three-body angular interactions along the backbone of the rings (Table III).

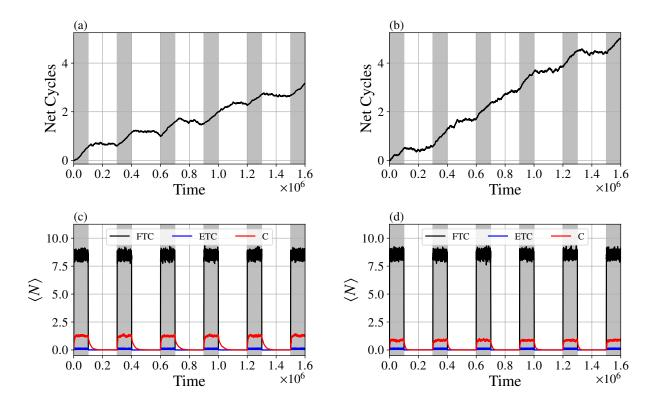


FIG. 10. The response of Motor I (a) and Motor II (b) to periodically varying $\mu'_{\rm FTC}$. Net cycles are defined as the number of clockwise cycles minus the number of counterclockwise cycles. The composition of the Motor I system (c) and Motor II system (d) with periodically varying $\mu'_{\rm FTC}$. Average numbers of FTC, ETC, and C are shown as a function of simulation time. The FTC chemical potential switches between $\mu'_{\rm FTC}=0.5$ for 1×10^5 units of time (gray shaded regions) to $-\mu'_{\rm FTC}=-10$ for 1×10^5 for 2×10^5 units of time (unshaded regions) and then the cycle repeats. Data shown are averages taken over 200 independent simulations.

Particle Type	m_i	σ_i	
BIND	1.0	1.0	
INERT	1.0	1.0	
CAT1	1.0	1.0	
CAT2	1.0	1.0	
CAT3	1.0	1.0	
SHUTTLE	1.0	1.0	
TET1	1.0	1.0	
TET2	1.0	1.0	
TET3	1.0	1.0	
TET4	1.0	1.0	
CENT	1.0	0.45	

TABLE I. All particles have unit radius and unit mass except for the central particle, which has a smaller radius.

Interaction	$\epsilon_{\mathrm{R},ij}$	$\epsilon_{ ext{A},ij}$	Bond Type	k_{ij}	$r_{\max,ij}$
TET*-TET*	10.0	0.0	harmonic	120.0	-
INERT-INERT	1.0	0.0	FENE	30.0	1.5
INERT-BIND	1.0	0.0	FENE	30.0	1.5
BIND-CAT2	1.0	0.0	FENE	30.0	1.5
CAT2-CAT1	1.0	0.0	FENE	30.0	1.5
CAT1-CAT3	1.0	0.0	FENE	30.0	1.5
CAT3-INERT	1.0	0.0	FENE	30.0	1.5
SHUTTLE-SHUTTLE	1.0	0.0	FENE	30.0	1.5
SHUTTLE-CAT1	1.0	0.0	none	-	-
SHUTTLE-CAT2	1.0	0.0	none	-	-
SHUTTLE-CAT3	1.0	0.0	none	-	-
SHUTTLE-TET*	500000.0	0.0	none	-	-
SHUTTLE-CENT	100000.0	0.0	none	-	-
SHUTTLE-INERT	1.0	0.0	none	-	-
INERT-TET*	1.0	0.0	none	-	-
INERT-CENT	1.0	0.0	none	-	-
INERT-CAT1	1.0	0.0	none	-	-
INERT-CAT2	1.0	0.0	none	-	-
BIND-BIND	1.0	0.0	none	-	-
BIND-CAT1	1.0	0.0	none	-	-
BIND-CAT3	1.0	0.0	none	-	-
BIND-TET*	1.0	0.0	none	-	-
BIND-CENT	1.0	0.0	none	-	-
CAT1-CAT1	1.0	0.0	none	-	-
CAT2-CAT2	1.0	0.0	none	-	-
CAT2-CAT3	1.0	0.0	none	-	-
CAT3-CAT3	1.0	0.0	none	-	-
TET*-CENT	1.0	0.0	none	-	-
CENT-CENT	100000.0	0.0	none	-	-
BIND-SHUTTLE	1.0	0.8 0.7	none	-	-
CAT1-TET1	0.888468	0.7328772	none	-	-
CAT1-TET2	1.215096	0.5734710	none	-	-
CAT1-TET3	1.424995	0.2213622	none	-	-
CAT1-TET4	0.216518	0.5113107	none	-	-
CAT1-CENT	2.798031	4.0973389 3.9229033	none	-	-
CAT2-TET1	1.153983	0.4533399	none	-	-
CAT2-TET2	4.138882	1.7037981	none	-	-
CAT2-TET3	1.073067	1.5169752	none	-	-
CAT2-TET4	0.560281	0.8455581	none	-	-
CAT2-CENT	1.824090	1.456227	none	-	-
CAT3-TET1	2.973898	1.3987962	none	-	-
CAT3-TET2	1.735298	2.0515572	none	-	-
CAT3-TET3	1.808303	0.2544759	none	-	-
CAT3-TET4	3.437772	1.4306526	none	-	-
CAT3-CENT	1.019612	0.931202	none	-	-

TABLE II. Pairwise interaction parameters for both modified Lennard-Jones interactions (Eq. 10) and bonding interactions. Vertices of the tetrahedra are linked with harmonic bonds while neighboring particles around the two rings are bonded together with FENE (finitely extensible nonlinear elastic) bonds in the order: BIND, CAT2, CAT1, CAT3, 11 INERT, BIND, CAT2, CAT1, CAT3, 11 INERT. For harmonic bonds k_{ij} is that of Eq. 11 while for FENE it is the $k_{F,ij}$ of Eq. 12. The two bold entries report the value for Motor I | the value for Motor II. An asterisk in the particle name, e.g. TET*, indicates that the value is the same for TET1, TET2, TET3, and TET4.

Interaction	$k_{A,ijk}$	$\theta_{0,ijk}$
SHUTTLE-SHUTTLE-SHUTTLE	3.0	$\pi \left(1 - \frac{2}{N_{\text{shuttle}}}\right)$
BIND-CAT2-CAT1	10.0	$\pi \left(1 - \frac{2}{N_{ m large}}\right)$
CAT2-CAT1-CAT3	10.0	$\pi \left(1 - \frac{2}{N_{\text{large}}}\right)$
CAT1-CAT3-INERT	10.0	$\pi \left(1 - \frac{2}{N_{\text{large}}}\right)$
CAT3-INERT-INERT	10.0	$\pi \left(1 - \frac{2}{N_{\text{large}}}\right)$
INERT-INERT-INERT	10.0	$\pi \left(1 - \frac{2}{N_{\text{large}}}\right)$
INERT-INERT-BIND	10.0	$\pi \left(1 - \frac{2}{N_{\text{large}}}\right)$
INERT-BIND-CAT2	10.0	$\pi \left(1 - \frac{2}{N_{\text{large}}}\right)$

TABLE III. Angular interaction parameters for Eq. (13). Note that the angular interactions are symmetric about the center particle such that $k_{A,ijk}$ would be equivalent to $k_{A,kji}$.